Superplasticity of metastable ultrafine-grained Ti−6242S alloy: Mechanical flow behavior and microstructural evolution

Hiroyuki Imai[a], Gen Yamane[a], Hiroaki Matsumoto[a,*], Vanessa Vidal[b], Vincent Velay[b]

[a] Department of Advanced Materials Science, Faculty of Engineering and Design, Kagawa University, 2217-20 Hayashi-cho, Takamatsu, Kagawa 761-0396, Japan
[b] Université de Toulouse, CNRS Mines Albi, INSA, ISAE, ICA (Institut Clément Ader), Campus Jarlard, 81013 ALBI Cedex 09, France

A B S T R A C T

Herein we quantitatively clarify the effects of grain size, β fraction, and morphology on the high-temperature deformation behavior of the Ti−6Al−2Sn−4Zr−2Mo–0.1Si alloy. For this purpose, five materials were subjected to high-temperature tensile deformation: the UFG1 specimen (having an equiaxed morphology with d_α = 0.78 μm and V_β = 2.8%), the UFG2 specimen (having an equiaxed morphology with d_α = 0.99 μm and V_β = 24.2%), the FG1 specimen (having an equiaxed morphology with d_α = 2.65 μm and V_β = 11.2%), the FG2 specimen (having an equiaxed morphology with d_α = 4.12 μm and V_β = 11.0%), and the STQ specimen (with an acicular α′ martensite morphology). The UFG1 specimen is produced by hot-rolling of the STQ specimen having an acicular α′ martensite microstructure at 750 °C. The UFG2 specimen is prepared by heat treatment of the UFG1 specimen at 400 °C. The FG1 specimen is as-received Ti−6242S alloy plate, and the FG2 specimen was prepared by heat treatment of the FG1 specimen at 900 °C. The UFG specimens exhibited higher ductility associated with frequent activation of superplasticity than the FG specimens owing to the effect of decreasing grain size. The STQ specimen exhibited higher ductility at 700 °C than the FG specimens. Quantitative analysis of the deformation mode according to internal-variable theory revealed much more grain boundary sliding in the UFG specimens. A comparison of the deformation behavior of the UFG1 and UFG2 specimens revealed excellent superplastic ductility in the UFG2 specimen at higher strain rates (10^{-3} and 10^{-2} s^{-1}) and in the UFG1 specimen at lower strain rates (5×10^{-4} and 10^{-4} s^{-1}). This behavior is ascribed mainly to different accommodation mechanisms during deformation of these specimens; dynamic β precipitation from supersaturated α microstructure occurred in the UFG1 specimen, whereas a decomposition process in which supersaturated β precipitates dissolve into the α phase was enhanced in the UFG2 specimen. In addition, the excess β precipitation observed in the UFG2 specimen led to enhanced α/β grain boundary sliding, resulting in further enhancement of the superplasticity.

Keywords:
Ti–6Al−2Sn−4Zr−2Mo–0.1Si alloy
Superplasticity
Ultrafine-grained microstructure
Metastable microstructure
Grain-boundary-sliding
Accommodation mechanism

1. Introduction

Titanium alloys have high specific strength and good corrosion resistance. The most widely used Ti alloy is Ti−6Al−4V owing to its good strength–ductility balance and excellent superplasticity. Among Ti alloys for aerospace applications, such as turbine engine and airframe applications, Ti−6Al−2Sn−4Zr−2Mo–0.1Si (Ti−6242S) was developed in the late 1960s and exhibits superior creep properties. Ti−6242S alloy is classified as a near-α alloy with a β phase content of 10–15% depending on the processing and heat treatment. Earlier studies [1,2] have indicated that the initial microstructure affects the creep properties of Ti−6242S alloy. In addition, Viswanathan et al. [3] described the mechanism of the creep behavior in detail, and they reported that the creep behavior at a stress of 172 MPa and temperatures of 538 and 565 °C was dominated by Harper–Dorn creep.

Net-shape processing of Ti alloys (such as isothermal forging of billets into products with complicated shapes and superplastic forming of sheets) should be performed under plastic deformation conditions at high temperatures of more than 850 °C and low strain rates. In practical terms, enhanced superplastic behavior at lower temperatures and higher strain rates is highly desirable. To enhance the superplasticity, refinement of the microstructure in the Ti−6Al−4V alloy has contributed to a decrease in the superplastic temperature to less than 800 °C and an increase in the required strain rate to more than 10^{-3} s^{-1}, which was associated with frequent grain boundary sliding (GBS). In fact, Ti−6Al−4V alloys having ultrafine-grained (UFG) microstructure produced by various processing routes exhibited high strain rate sensitivity (0.35–0.65) and excellent high-temperature ductility

* Corresponding author.
E-mail address: matsu_h@eng.kagawa-u.ac.jp (H. Matsumoto).

Table 1
Summary of characters of specimens and process-routes.

Specimens	Characters of Experimental procedure	Memo
FG1	As-received Ti−6242S alloy plates.	Average α size: 2.65 μm
FG2	Heat-treated FG1 specimen at 900 °C for 36 ks and cooled in the furnace.	Average α size: 4.12 μm
STQ	Solution-treated as-received 4-mm-thick Ti−6242S alloy plate at 1100 °C for 1.8 ks and quenched in ice water.	Microstructure: α′martensite microstructure.
UFG1	Hot-rolled STQ specimens at 750 °C to approximately 1.3 mm by five passes (a reduction of 0.5 mm per pass).	Average α size: 0.78 μm
UFG2	Heat-treated UFG1 specimens at 400 °C for 10.8 ks.	Average α size: 0.99 μm

under testing at lower temperatures ranging from 650 to 800 °C [4–8]. Cope et al. [9] and Park et al. [10] have reported the deformation behavior of superplastic Ti−6242S alloy in detail. As in the deformation behavior of the Ti−6Al−4V alloy, grain size refinement of the Ti−6242S alloy has contributed to enhanced GBS, resulting in enhanced superplasticity. Regarding the GBS in superplastic deformation of the (α + β) Ti alloy, the α/β phase ratio is an important factor that influences the superplastic behavior. The β phase is well known to act as an accommodation mechanism during superplasticity, and a volume fraction of 20% is estimated to be optimal for superplastic deformation [11]. The reason is the suppression of grain growth of the α phase and easier GBS at the α/β boundary [12,13].

During tensile deformation of metallic alloys at high temperatures, dynamic recovery and/or dynamic recrystallization (DRX) occur, resulting in microstructural conversion [14]. There are two types of DRX: discontinuous dynamic recrystallization, in which new grains are formed by heterogeneous nucleation and growth, and continuous dynamic recrystallization (CDRX), in which subgrains with low-angle boundaries are formed and subsequently evolve into grains with a high fraction of high-angle boundaries with increasing strain. It is well recognized that CDRX is frequently activated in hot deformation of (α + β) Ti alloys [15–17]. We recently reported that CDRX of coarse grains retained in the heterogeneous UFG microstructure during hot deformation acted as an additional accommodation mechanism and resulted in enhanced GBS [8]. Additionally, β precipitation during superplastic deformation reportedly acts as an additional stress accommodation mechanism at grain boundaries [7,18].

In contrast to the case of Ti−6Al−4V alloy, few reports on the Ti−6242S alloy mention the superplastic deformation behavior of specimens having UFG microstructure with grain sizes of less than 1 μm. Further, the effect of initial metastable microstructure with various β fractions on the plastic flow behavior is unclear. Therefore, this work examines the deformation behavior of UFG Ti−6242S alloy. It focuses on quantitative analysis of the effects of grain size and morphology on the high-temperature tensile deformation mode and microstructural evolution of UFG Ti−6242S alloy and fine-grained (FG) Ti−6242S alloy. The main objectives are as follows.

- Ti−6242S alloy having an equiaxed UFG microstructure is produced via controlled hot rolling of the initial α′ martensite microstructure, and the high-temperature tensile deformation mode is evaluated in detail.
- The effect of changes in β fraction on the high-temperature deformation mode of UFG Ti−6242S alloys with a metastable initial condition is evaluated.
- The deformation behavior of FG Ti−6242S alloys having average grain sizes of 2–5 μm are compared with the behavior of the UFG Ti−6242S alloys.
- Additionally, to examine the effect of the initial microstructure on the deformation behavior, the tensile behavior of Ti−6242S alloy with an acicular α′ martensite initial microstructure is also examined.

2. Experimental procedure

2.1. Materials

Ti−6242S alloy with a chemical composition (in wt%) of 6.02Al, 2.0Sn, 4.1Zr, 2.01Mo, 0.09Si, 0.1O, 0.02N, and balance Ti was used. An as-received 4-mm-thick Ti−6242S alloy plate having an equiaxed (α + β) microstructure was solution-treated at 1100 °C for 1.8 ks and quenched in ice water to obtain α′ martensite microstructure. The quenched specimen with α′ martensite microstructure is referred to as the STQ specimen. The 4-mm-thick STQ specimen was hot-rolled at 750 °C to a thickness of approximately 1.3 mm by five passes (a reduction of 0.5 mm per pass) to obtain UFG microstructure. This hot-rolled specimen is referred to as the UFG1 specimen. To control the β fraction while maintaining the UFG morphology, the UFG1 specimen was heat-treated at a low temperature of 400 °C for 10.8 ks. This heat-treated specimen is referred to as the UFG2 specimen. Additionally, the as-received Ti−6242S alloy with an average α grain size of 2.65 μm (the FG1 specimen) was heat-treated at 900 °C for 36 ks and cooled in the furnace to control the grain growth. The heat-treated Ti−6242S alloy is referred to as the FG2 specimen (average α grain size: 4.12 μm). The UFG1 and UFG2 specimens are collectively referred to as the UFG specimens, and the FG1 and FG2 specimens are collectively referred to as the FG specimens. Table 1 summarizes the characters of specimens and process-routes.

2.2. Microstructure

The microstructure was observed using a JEOL JSM-7001F field emission gun scanning electron microscope (SEM) equipped with an Oxford-HKL electron backscatter diffraction (EBSD) detector. The crystallographic orientation and fraction of low-angle boundaries were evaluated using EBSD. Samples for SEM-EBSD observation were prepared by mechanical polishing followed by final polishing with a 0.06 μm colloidal suspension for 3.6 ks.

2.3. Evaluation of high-temperature deformation behavior

Tensile tests in air atmosphere were performed at temperatures ranging from 650 to 900 °C and initial strain rates ranging from 1×10^{-4} to 1×10^{-2} s^{-1}. Tensile specimens, with a gauge length of 5 mm, width of 2 mm, and thickness of 1.3 mm, were machined to be parallel to the final rolling direction of the plate. The surface of the tensile specimens was coated with oxidation-resistant glass before heating to reduce the influence of oxidation as much as possible. The testing conditions are summarized in Table 2. Additionally, tensile tests of the FG1 specimen were also conducted at 730, 750, and 920 °C (open circles in Table 2) using a tensile specimen with a gauge length of 20 mm and width of 8 mm [19]. The strain rate sensitivity m was determined by evaluating the slope of log σ (at a true plastic strain of 0.1)–log $\dot{\varepsilon}$ curves or the strain rate change test. To evaluate m at a later stage of deformation according to the strain rate change test, specimens were deformed under a constant crosshead speed corresponding to an initial strain rate of 10^{-2} s^{-1} up to a true plastic strain of nearly 0.4, followed by consecutive stepwise changes to constant true strain rates of 5×10^{-3}, 10^{-3}, 5×10^{-4}, and 10^{-4} s^{-1}.

Table 2
Tensile test conditions in this work (✓)and in other works (○) according to Ref. [19]. The strain rate ranges from 1×10^{-4} to 1×10^{-2} s^{-1}.

Temperature	Specimen				
	UFG1	UFG2	FG1	FG2	STQ
650 °C	✓				✓
700 °C	✓	✓	✓	✓	✓
730 °C			○		
750 °C	✓		○		
800 °C	✓	✓	✓	✓	✓
840 °C			○		
900 °C			✓	✓	
920 °C			○		

2.4. Load relaxation test

Load relaxation tests were performed to obtain the relationship between the stress and strain rate. A specimen with a gauge length of 12 mm, width of 4 mm, and thickness of 1.8 mm was tested at temperatures of 700 and 800 °C. In this test, a small amount (10%) of nominal plastic strain was applied to the specimen at an initial strain rate of 5×10^{-2} s^{-1}, and the strain was held constant, resulting in load relaxation. The obtained load–time curves were converted into stress–strain rate curves by the method of Lee and Hart [20]. On the basis of these results, the constitutive parameters for the internal-variable model [21] were determined by nonlinear regression analysis. This internal-variable model enables quantitative analysis of the GBS. By using this approach, the deformation mode of Al alloys [22] and Ti alloys [10,12,23,24] has been quantitatively analyzed.

3. Results

3.1. Initial microstructure before tensile test

On Fig. 1, EBSD orientation images in the normal direction to the rolling plane (ND direction) and SEM–backscattered electron (BSE) images, reveal the initial microstructure of the UFG1 and UFG2 specimens before tensile deformation. The average grain size, β fraction, and fraction of high-angle grain boundaries (f_{HAGB}) are also shown. The microstructure of both the UFG1 and UFG2 specimens consists mainly of ultrafine equiaxed grains with an average grain size of less than 1 μm. In the microstructures, coarse deformed grains corresponding to un-DRX grains are also observed a little. The estimated average grain sizes are 0.78 μm and 0.99 μm for the UFG1 and UFG2 specimens, respectively. As described below, the FG specimen in equilibrium exhibits a β fraction of approximately 11%. The SEM-BSE images in Figs. 1(a-2) and (b-2) show that, compared to this equilibrium β fraction, there are fewer β precipitates in the UFG1 specimen and more β precipitates in the UFG2 specimen, indicating that both UFG specimens have metastable microstructure. For the UFG1 specimen, β precipitation during processing is assumed to be retarded because the initial microstructure consists of the single α′ martensite phase having hexagonal close-packed structure. On the other hand, the excessive β precipitation in the UFG2 specimen is thought to be attributable to a very high driving force for β precipitation under aging at 400 °C resulting from very densely accumulated dislocations in the specimen before aging. Furthermore, it can be observed from Fig. (b-2) that β phase is heterogeneously distributed as aggregated morphology. With respect to the microstructural formation in the UFG2 specimen, further experiments are underway to identify it.

Fig. 2(a), (b), and (c) show SEM-BSE images of the microstructure of the FG1, FG2, and STQ specimens, respectively. The FG1 and FG2 specimens exhibit equiaxed microstructure having a β fraction of approximately 11%. The average grain size of the FG1 specimen is approximately 2.65 μm, and that of the FG2 specimen is approximately 4.12 μm. In contrast, acicular α′ martensite microstructure is observed in the STQ specimen.

3.2. Flow behavior and elongation to fracture

Typical flow curves obtained at 700 and 800 °C and a strain rate of 10^{-3} s^{-1} are shown in Fig. 3. At 700 °C [Fig. 3(a)], extensive flow softening is clearly observed for the FG1 and FG2 specimens. Additionally, the STQ specimen exhibits higher elongation than the FG specimens. We mentioned recently that Ti−6Al−4V alloy having initial α′ martensite microstructure exhibited excellent high-temperature tensile ductility, owing mainly to enhanced dynamic globularization, which acted as an additional accommodation mechanism [25]. In fact, similar enhancement of the dynamic globularization during deformation is experimentally confirmed for the STQ specimen of Ti−6242S alloy in this work; therefore, this enhancement results in the higher ductility of the STQ specimen at 700 °C. As the grain size decreases to less than 1 μm, the UFG specimens exhibit much higher tensile ductility. Specifically, the UFG2 specimen exhibits lower flow stress and higher elongation than the UFG1 specimen, even though both UFG specimens exhibit close ultrafine average grain sizes. This result indicates that the excessive β phase formation observed in the UFG2 specimen contributes to enhancement of the easier α/β GBS, resulting in lower flow stress and higher ductility. In contrast, at 800 °C [Fig. 3(b)], there is no apparent difference in the flow stress and total elongation to fracture between the UFG1 and UFG2 specimens, indicating that the amount of β precipitates in the initial microstructure has a lower effect on flow behavior than at 700 °C. In addition, we can observe steady-state deformation followed by gradual flow softening behavior and high ductility for both FG specimens, as shown in Fig. 3(b), indicating that obvious superplasticity occurs for the FG specimens at 800 °C.

Fig. 4 summarizes the elongation to fracture of the UFG, FG, and

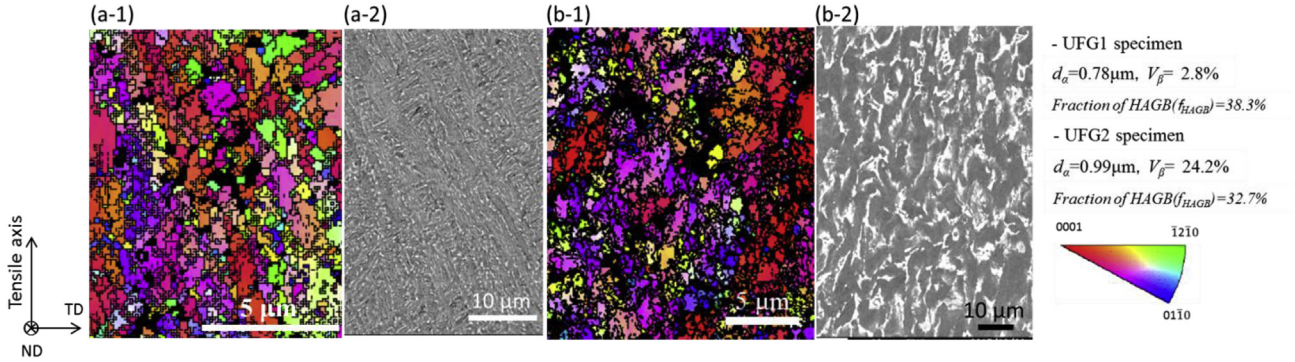

Fig. 1. Microstructure of (a-1), (a-2) UFG1 specimen and (b-1), (b-2) UFG2 specimen as shown by EBSD orientation images [(a-1) and (b-1)] and SEM-BSE images [(a-2) and (b-2)]. In the EBSD orientation images, the black regions correspond to grain boundaries and β phase.

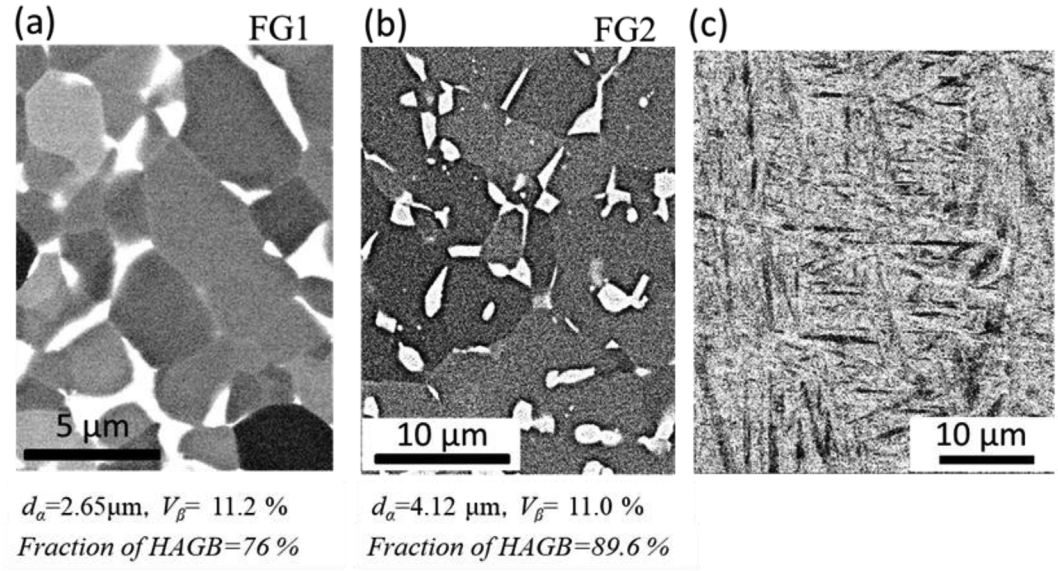

Fig. 2. SEM-BSE images of (a) FG1 specimen, (b) FG2 specimen, and (c) STQ specimen.

STQ specimens at various temperatures and strain rates. As mentioned above, for all the strain rates at 700 °C, the STQ specimen exhibits higher elongation values (approximately 100%) than the FG specimens, which is attributable to enhancement of the accommodation mechanism associated with the frequent occurrence of dynamic globularization associated with frequent occurrence of DRX from α′ martensite. The UFG specimens exhibit much higher elongation than the FG specimens, owing mainly to the effect of smaller initial grain size. The UFG2 specimen tends to exhibit higher elongation at higher strain rates ($\geq 10^{-3}\,s^{-1}$ at 700 °C and $\geq 5 \times 10^{-4}\,s^{-1}$ at 800 °C), and the UFG1 specimen exhibits higher elongation at lower strain rates. That is, this result indicates that the UFG1 and UFG2 specimens have different deformation modes depending on the strain rate, even though they both have ultrafine average grain sizes. This behavior is discussed in detail in a later section. Additionally, both UFG specimens show a decrease in elongation with decreasing strain rate from 5×10^{-4} to $1 \times 10^{-4}\,s^{-1}$ at 800 °C. During deformation at high temperature and low strain rate, dynamic grain growth obviously occurs, and the measured grain sizes of the specimens after tensile fracture at 800 °C and $10^{-4}\ s^{-1}$ are 4.3 μm for the UFG1 specimen and 4.0 μm for the UFG2 specimen. Thus, the dynamic grain growth observed in the UFG specimens results in decreasing the high-temperature ductility owing to a decrease of the GBS.

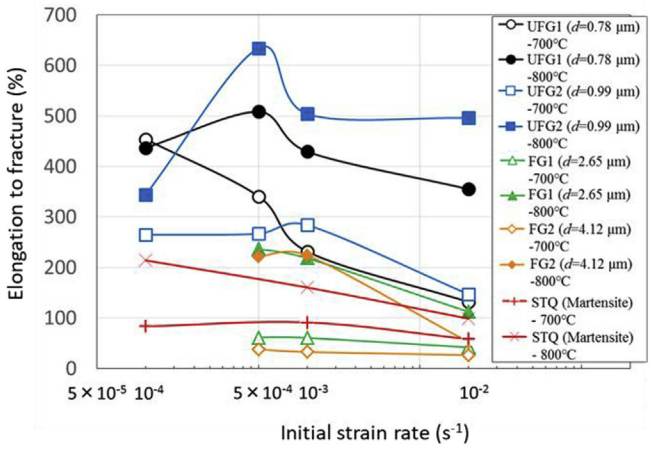

Fig. 4. Elongation to fracture of all specimens as a function of strain rate at 700 and 800 °C.

3.3. Kinetic analysis of high-temperature tensile deformation

The deformation behavior of the Ti—6242S alloys with various types of initial microstructure will be discussed according to kinetic analysis

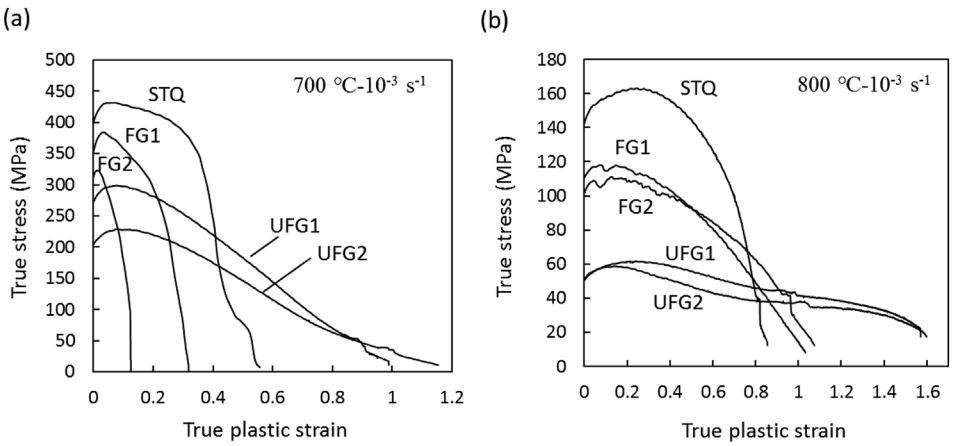

Fig. 3. True stress – true plastic strain curves of UFG, FG, and STQ specimens at $10^{-3}\ s^{-1}$ and (a) 700 °C and (b) 800 °C.

Table 3
Summary of the strain rate sensitivity m at 700 and 800 °C of the UFG, FG, and STQ specimens as estimated at $\varepsilon_P = 0.1$ and evaluated by strain rate jump testing at $\varepsilon_P > 0.4$.

	700 °C	800 °C	800 °C[a]
	m (at the $\varepsilon_P = 0.1$)	m (at the $\varepsilon_P = 0.1$)	m (at the $\varepsilon_P \geq 0.4$)
UFG1	0.36	0.41	0.47
UFG2	0.31	0.36	0.38
FG1	0.16	0.31	0.42
FG2	0.15	0.18	0.47
STQ	0.19	0.25	

[a] Evaluation by strain rate jump test.

of the deformation. A strain rate sensitivity $[m = \delta(\ln\sigma)/\delta(\ln\dot{\varepsilon})]$ of more than 0.3 is seen for superplastic deformation. The estimated m values at a plastic strain (ε_P) of 0.1 at 700 and 800 °C and the m values evaluated by strain rate jump testing at a plastic strain above 0.4 at 800 °C are summarized in Table 3. According to the estimated m values at $\varepsilon_P = 0.1$, m is higher (> 0.3) for the UFG specimens at both 700 and 800 °C and for the FG1 specimen at 800 °C, indicating that superplasticity occurs under these conditions. The m values also increase with increasing testing temperature from 700 to 800 °C. This result indicates that activity of GBS increases with increasing temperature. Additionally, the STQ specimen exhibits a higher m value at 700 °C than the FG specimens, which is quite consistent with the elongation-to-fracture result (Fig. 4). To clarify the effect of strain on m, a tensile strain rate jump test at 800 °C was also performed at $\varepsilon_P \geq 0.4$. The obtained m values are higher than those obtained at $\varepsilon_P = 0.1$ for all the specimens, suggesting that dynamic microstructural change during deformation contributes to increased GBS. For the UFG specimens, the increase in m from $\varepsilon_P = 0.1$ to $\varepsilon_P \geq 0.4$ is greater in the UFG1 specimen. As described below, for the UFG1 specimen, dynamic β precipitation, which frequently occurs with increasing strain, is deduced to effectively contribute to an additional accommodation mechanism of stress concentration.

The apparent activation energy Q for hot deformation is determined by assuming the strain rate follows an Arrhenius-type equation, as follows:

$$\dot{\varepsilon} = A\sigma^n \exp\left(-\frac{Q}{RT}\right) \tag{3–1}$$

where A is the material constant, R is the gas constant, and $n = 1/m$ is the stress exponent. The estimated Q values are 358 kJ/mol (UFG1), 356 kJ/mol (UFG2), 383 kJ/mol (FG1), 413 kJ/mol (FG2), and 442 kJ/mol (STQ). The Q values reported in the literature [4,11,26] for (α + β) Ti−6Al−4V alloy range from 300 to 330 kJ/mol. Further, the reported Q values for creep deformation of Ti−6242S alloy range from 298 to 374 kJ/mol [27]. These reported values are close to the estimated Q values, indicating that high-temperature deformation of the UFG and FG specimens is associated with thermally activated dislocation motion. The higher Q value of 442 kJ/mol for the STQ specimen is attributable to the frequent occurrence of dynamic globularization during deformation.

Next, we discuss the active deformation mode in relation to the Zener–Hollomon (Z) parameter, a temperature-compensated strain rate used for kinetic analysis. The Z parameter is given by

$$Z = \dot{\varepsilon}\exp\left(\frac{Q}{RT}\right) \tag{3–2}$$

where R is the gas constant [8.314 J/(mol K)], T is the absolute temperature, and Q is the activation energy calculated as described above. Fig. 5(a) shows the relationship between the flow stress at $\varepsilon_P = 0.1$ and log(Z). Linear relationships are clearly observed for all the specimens, revealing that deformation occurs by a thermally activated process. The UFG specimens exhibit quite similar relationships, indicating that the active deformation mode is similar for both specimens. The FG specimens show two slopes in the lower log(Z) region (dotted line) and higher log(Z) region (solid line), suggesting that the dominant deformation mode depends on the testing conditions associated with the change in the Z parameter. Here, the magnitude of the slope in the lower log(Z) region for the FG specimens is similar to that of the slope for the UFG specimens, suggesting that superplasticity is enhanced in the lower log(Z) region for the FG specimens. On the other hand, for the STQ specimen, the deformation mode associated with frequent dynamic globularization is dominant, which is a different mode from that of the UFG specimens. Thus, it results in a lower magnitude of the slope for the STQ specimen, as shown in Fig. 5(a).

The relationship between the elongation to fracture and log(Z) is shown in Fig. 5(b). The elongation to fracture tends to decrease with increasing log(Z), which is related to the decrease in temperature and increase in strain rate. We can roughly identify two regions (Regions I and II) according to the behavior of the elongation to fracture. In Region I, Z depends significantly on the elongation, and much higher elongation appears at lower log(Z). In Region II, the elongation gradually decreases with increasing log(Z). Most of the results for the UFG specimens appear in Region I, whereas most of the results for the FG and STQ specimens appear in Region II. These results indicate that superplasticity, which is associated with excellent ductility, is notably enhanced under the deformation conditions in which log(Z) ranges from 13 to 17. In Fig. 5(b), Region I-2 also appears inside of Region I; it corresponds to the region in which the superplasticity is enhanced for the FG specimens. Indeed, as mentioned below, GBS shows notable enhancement in the process window of Region I-2 for the FG specimens.

4. Discussion

4.1. Characteristics of deformed microstructure

Next, we discuss the deformation mode according to the deformed microstructures. Fig. 6 shows SEM-BSE images of the UFG and FG specimens illustrating the microstructure after deformation at 10^{-3} s^{-1} and fracture. The black and white regions correspond to the α and β phases, respectively. Homogeneous equiaxed microstructure is observed for all the specimens. No obvious grain growth after deformation (compared to the grain size in the initial microstructure) is observed for any of the specimens tested at 700 °C. On the other hand, among the specimens tested at 800°, the UFG specimens, but not the FG specimens, exhibit grain growth. As mentioned below, this result is attributable to frequent activation of CDRX in the FG specimens under deformation at 800 °C.

Fig. 7 shows EBSD ND orientation images illustrating the microstructural evolution of the UFG specimens at 800 °C and 10^{-3} s^{-1} under true plastic strains of 0.4 and 0.69 and fracture strains of 1.67 for the UFG1 specimen and 1.80 for the UFG2 specimen. The colored and black regions correspond to the α and β phases, respectively. The UFG specimens exhibit similar evolution of the crystallographic orientation, in which the orientation becomes random and grain growth occurs with increasing strain. Further, f_{HAGB} increases significantly with strain. These results indeed indicate that GBS is the dominant deformation mode throughout deformation of the UFG specimens.

Fig. 8 shows the deformed microstructure of the FG specimens under various strains at 800 °C and 10^{-3} s^{-1}. Equiaxed microstructure remains even after large deformation. A comparison to the microstructure before deformation (Fig. 2) reveals that f_{HAGB} first decreases in the initial stage of deformation at a true plastic strain of 0.4 and then gradually increases. This result indicates that subgrain formation accompanied by frequent dislocation movement is dominant in the initial stage of deformation of the FG specimens. The FG1 specimen shows no apparent change in grain size up to a true plastic strain of 0.69 and a slight increase in grain size at a fracture strain of 1.16 compared to the

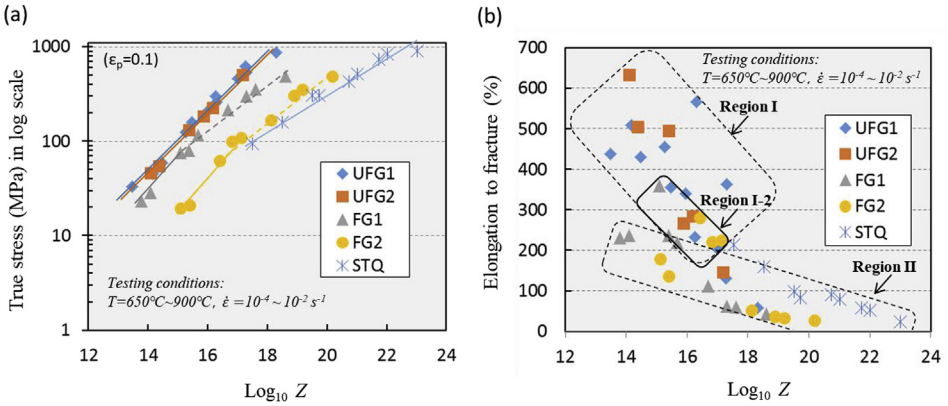

Fig. 5. (a) Relationship between the stress at ε_P = 0.1 and Z parameter (log–log scale) and (b) relationship between the elongation to fracture and Z parameter (log–log scale) at temperatures ranging from 650 to 900 °C and strain rates ranging from 10^{-4} to 10^{-2} s^{-1}.

initial microstructure before deformation [Fig. 2(a)]. On the other hand, the FG2 specimen exhibits refinement of α grains at a true plastic strain of 0.69, followed by continuous grain growth. This result suggests that CDRX occurs frequently at an intermediate stage of deformation for initial microstructure with grain sizes above 4 μm.

As mentioned above, there is no apparent difference in the deformed microstructure of the UFG1 and UFG2 specimens, as shown in Figs. 6 and 7, although the flow behavior (Fig. 3) and elongation to fracture (Fig. 4) of these two specimens do differ. Next, we discuss these findings using evaluation of the grain size and β precipitate evolution and quantitative analysis of the GBS.

4.2. Grain size evolution and β precipitate evolution

Fig. 9(a) and (b) show the grain size of the α phase after deformation as a function of true plastic strain (which corresponds to the fracture strain for each test condition) for the UFG1 and FG1 specimens, respectively. In Fig. 9(b), the results obtained at 730, 840, and 920 °C using the same FG1 specimen according to Ref. [19] are also presented. Regardless of the testing temperature, the UFG1 and FG1 specimens exhibit similar grain size evolution. That is, the grain size decreases under a plastic strain of approximately 0.8 and then gradually increases up to a plastic strain of approximately 1.5. At a plastic strain of approximately 1.5, a large deviation is observed depending on the testing

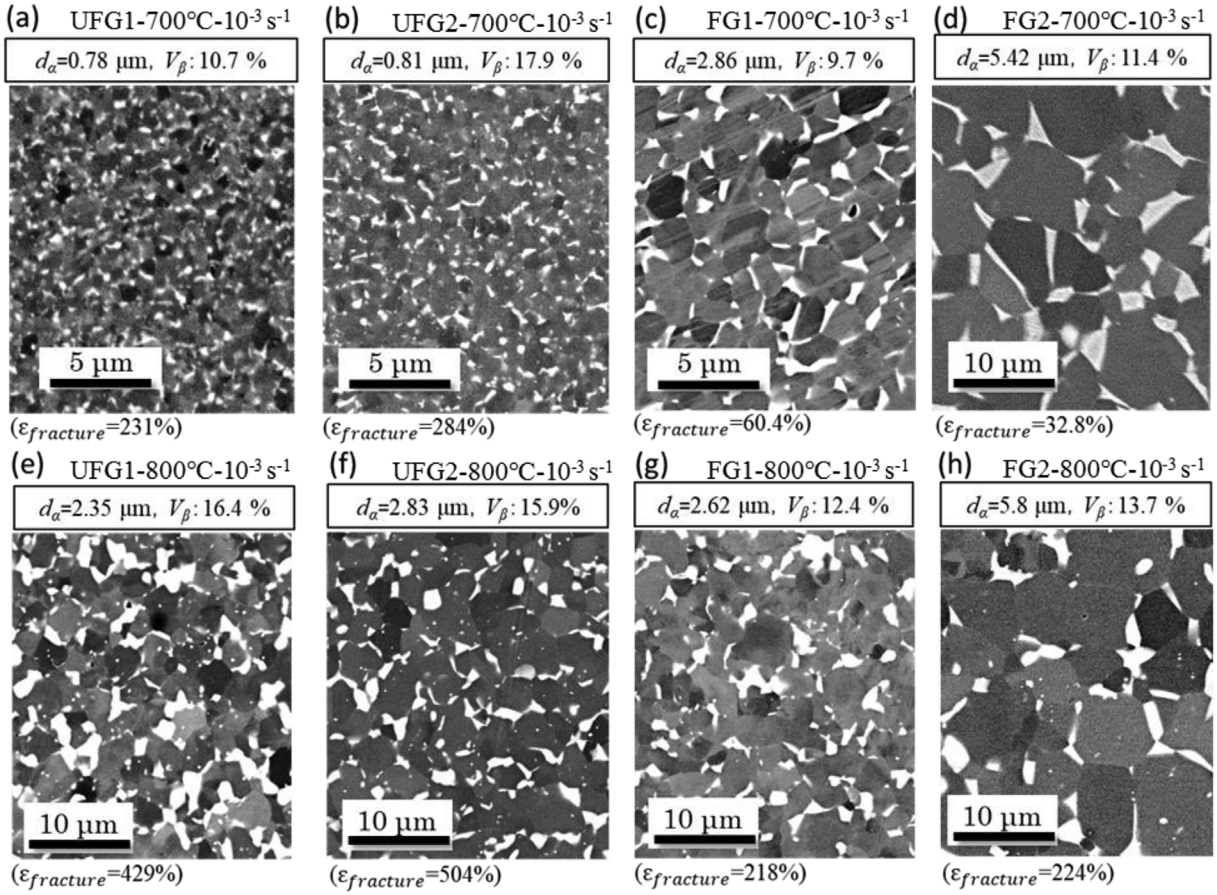

Fig. 6. SEM-BSE images showing deformed microstructure after tensile fracture of (a), (e) UFG1 specimen, (b), (f) UFG2 specimen, (c), (g) FG1 specimen, and (d), (h) FG2 specimen at 10^{-3} s^{-1} and (a)–(d) 700 °C and (e)–(h) 800 °C. Grain sizes of α phase and β fraction are also shown.

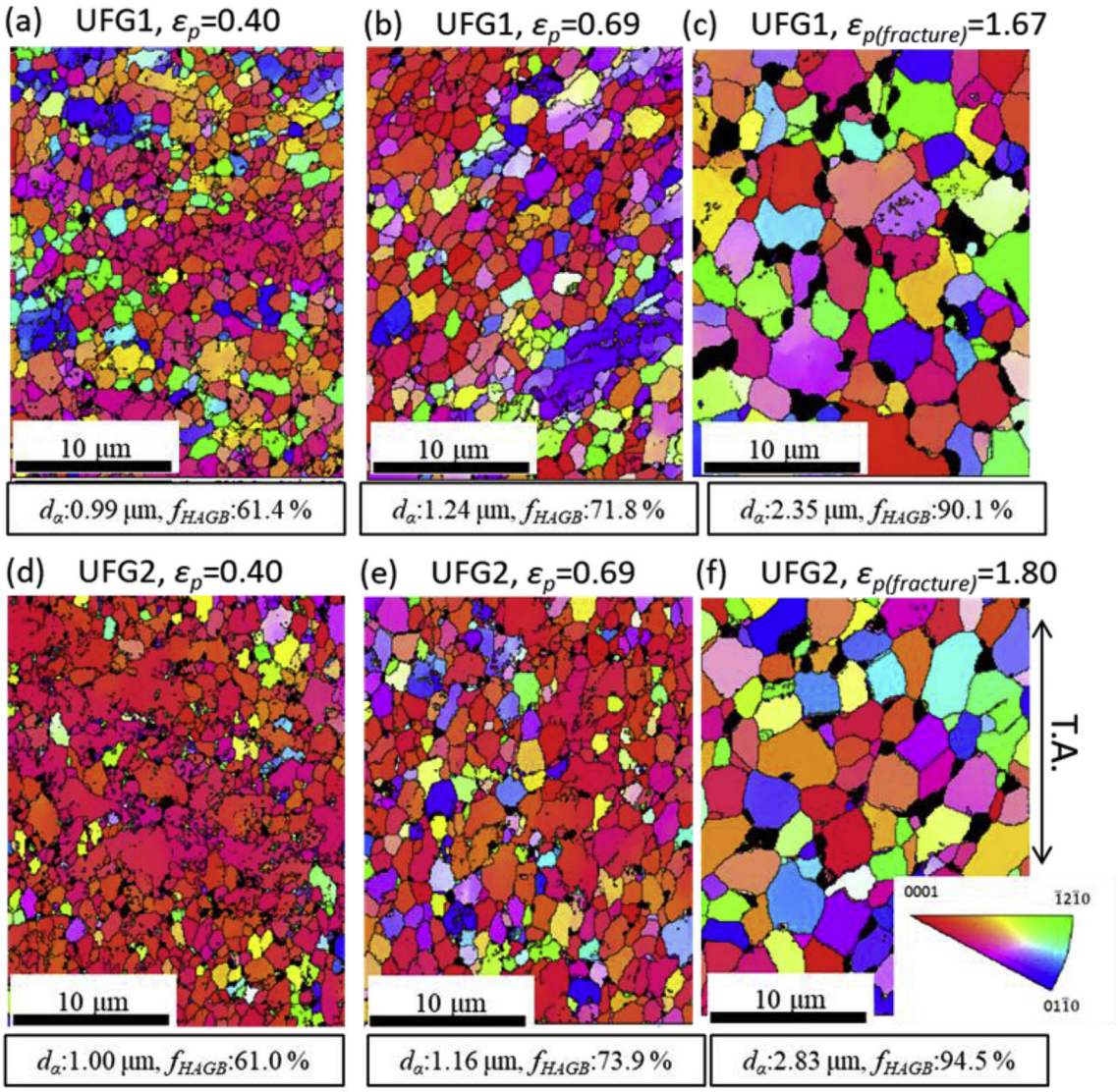

Fig. 7. EBSD ND orientation images showing deformed microstructure with various strains at 800 °C and 10^{-3} s^{-1} of (a)–(c) UFG1 specimen and (d)–(f) UFG2 specimen. The true plastic strains are (a), (d) 0.4, (b), (e) 0.69, (c) 1.67, and (f) 1.80.

temperature, in which the grains become coarser with increasing temperature. This result indicates that the effect of coarsening depending on the testing condition is strong in the high-strain region; here grain coarsening is significant at higher temperatures and lower strain rates. The observed microstructure suggests that the decrease in grain size observed at strains up to a plastic strain of approximately 0.8 is attributable mainly to frequent CDRX during deformation. Additionally, the decrease in grain size at $\varepsilon_P = 0.8$ is greater in the FG1 specimen. This clearly demonstrates that CDRX accompanied by dislocation glide is the dominant deformation mode in the initial and intermediate stages for the FG1 specimen.

Now we focus on β precipitate evolution during deformation. Fig. 10(a) and (b) show the β fraction in the gage section (deformed region) and grip section (undeformed region) after deformation of the FG and UFG specimens at 700 and 800 °C, respectively. Note that the β fraction in the initial condition before deformation is shown in Figs. 1 and 2. At 800 °C [Fig. 10(b)], similar β fractions ranging from 12% to 15% are seen in the gage section of all the specimens, indicating that the β fraction of all the specimens reaches that in the equilibrium condition at 800 °C. However, as shown in Fig. 10(a), the β fraction exhibits unique behavior under testing at 700 °C. For the FG specimens after deformation, the β fractions are similar (approximately 10%), and there is no apparent difference in the β fraction compared to the initial condition (approximately 11%, as shown in Fig. 2). This result suggests that the β fraction evolves under the equilibrium condition during deformation of the FG specimens. On the other hand, the β fraction of the UFG specimens evolves significantly; the β fraction in the gage section of the UFG2 specimen decreases dramatically after deformation compared to the β fraction before deformation (24.2%) and is lower than that in the grip section. In contrast, the β fraction in the gage section of the UFG1 specimen increases dramatically after deformation and is higher than that in the grip section. The above results for the behavior of the UFG specimens at 700 °C indicate a decomposition process in which dissolution of supersaturated β precipitates into the α phase is enhanced in the UFG2 specimen, and dynamic β precipitation at the triple junction of α grain boundaries is enhanced in the UFG1 specimen. As mentioned above, the excessive β phase precipitation observed in superplastic deformation of UFG Ti−6Al−4V alloy [7] and Ti−Al−Fe alloy [18] acted as an additional accommodation mechanism and contributed to the enhanced superplasticity. In light of these previous findings, the enhanced dissociation of the β phase from the initial metastable condition in the present UFG Ti−6242S specimens can be thought to contribute to an additional accommodation mechanism, thus leading to higher ductility.

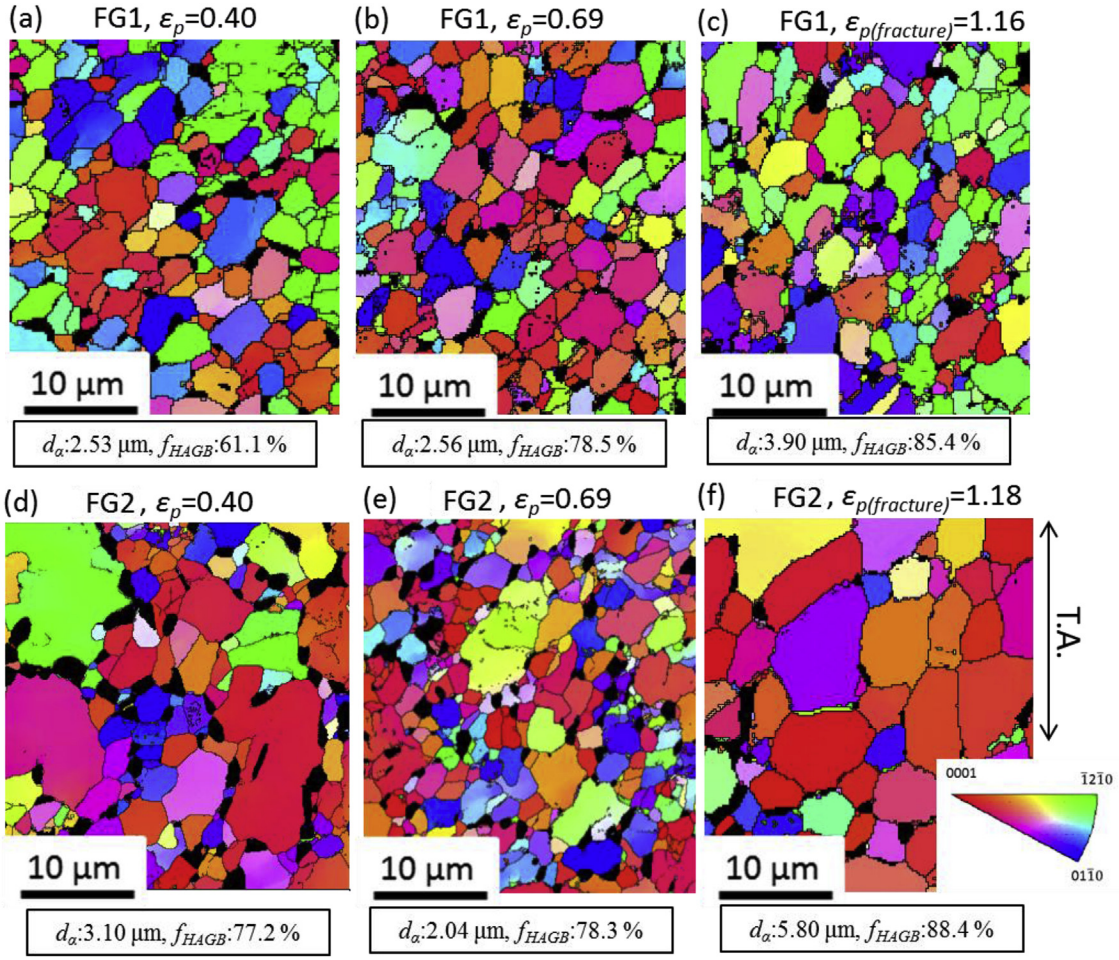

Fig. 8. EBSD ND orientation images showing deformed microstructure under various strains at 800 °C and 10^{-3} s^{-1} of (a)–(c) FG1 specimen and (d)–(f) FG2 specimen. The true plastic strains are (a), (d) 0.4, (b), (e) 0.69, (c) 1.16, and (f) 1.18.

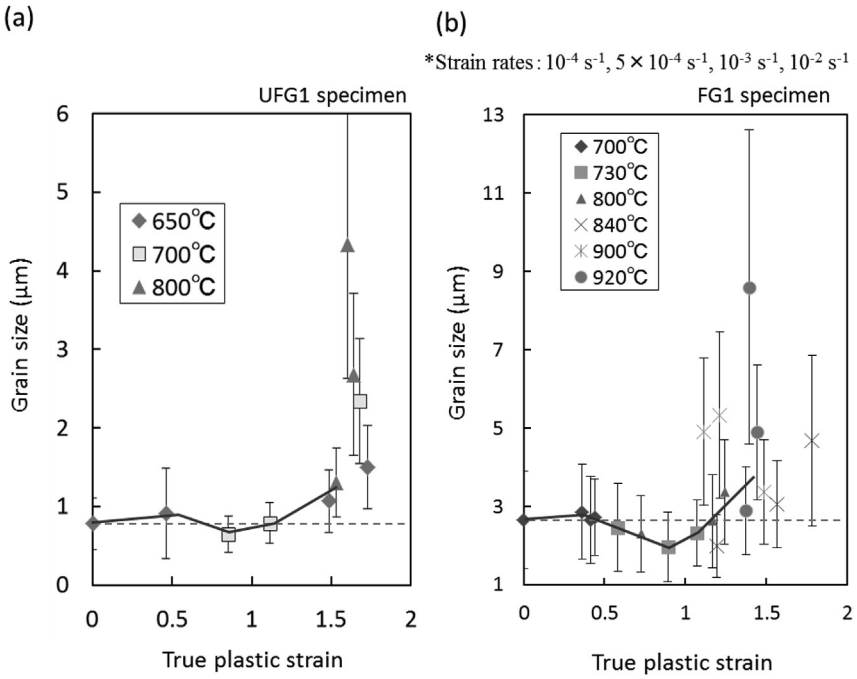

Fig. 9. Grain size evolution as a function of true plastic strain for (a) UFG1 specimen at 650, 700, and 800 °C and (b) FG1 specimen at 700–920 °C.

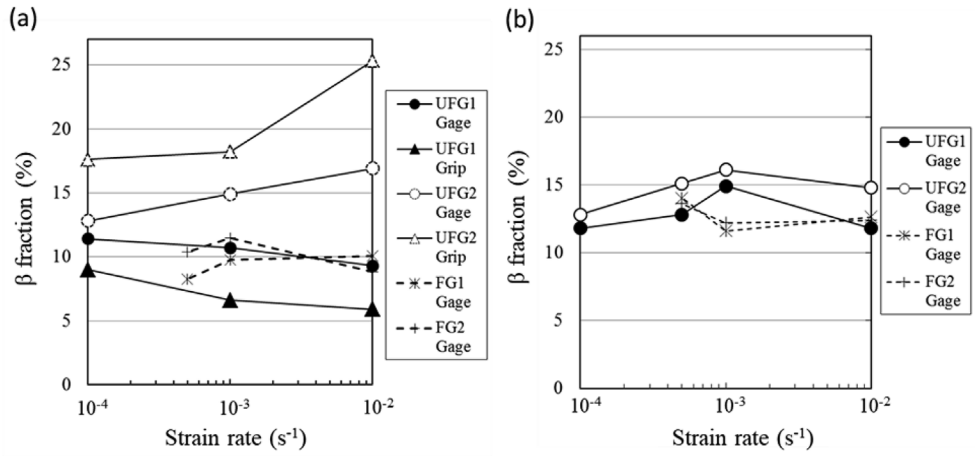

Fig. 10. β fraction as a function of strain rate of UFG and FG specimens after deformation at (a) 700 °C in the gage and grip sections and (b) 800 °C in the gage section.

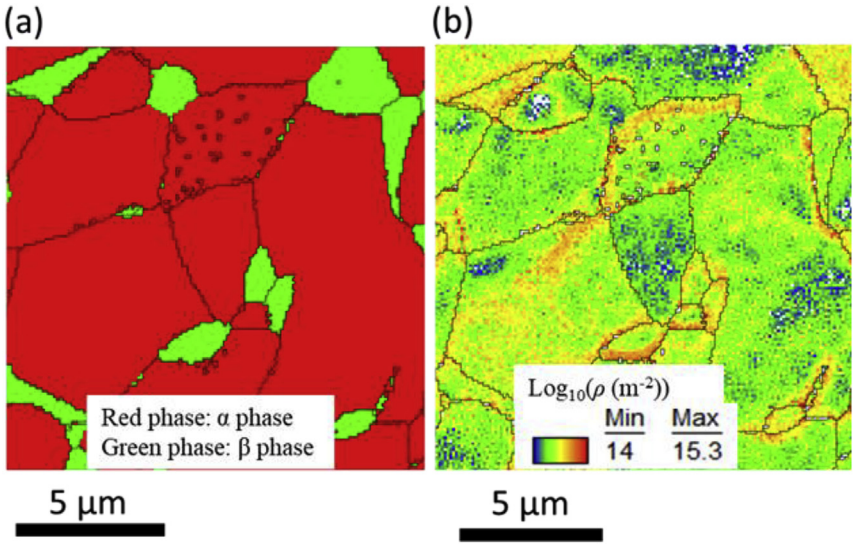

Fig. 11. (a) EBSD phase map and (b) distribution of the estimated GND density of UFG1 specimen after deformation at 800 °C and $10^{-4}\,s^{-1}$ at a true strain of 1.6.

Regarding the role of the β phase in superplastic deformation behavior, a β phase volume fraction of 20% is estimated to be optimal for superplastic deformation owing to the suppression of grain growth [11] and easier GBS at the α/β boundary [12,13]. Moreover, previous reports [28,29] have described the superplasticity of an α/β Ti−6Al−4V alloy having an average grain size of more than 3 μm in terms of the Gifkins core–mantle model [30], in which GBS occurred through the motion of grain boundary dislocations that accumulated at the triple point. Fig. 11(a) and (b) show EBSD images representing the phase map and distribution of geometrically necessary dislocations (GNDs) in the UFG1 specimen after tensile fracture at 800 °C and $10^{-4}\ s^{-1}$. A non-uniform plastic deformation is accompanied by the development of GNDs [31], which preserve the compatibility of the crystallographic lattice. According to Calcagnotto et al. [32], the equation for the local misorientation angle assumes a series of cylinder-torsion twist subgrain boundaries, each containing two perpendicular arrays of screw dislocations:

$$\rho_{GND} = \frac{2\Delta\theta}{\mu b} \tag{3-3}$$

where μ is the unit length (= 0.1 μm), and b is the magnitude of the Burgers vector (2.95×10^{-10} m for the α phase and 2.80×10^{-10} m for the β phase). Misorientations below 2° are excluded from the calculation because these points are thought to belong to adjacent grains or subgrains.

Fig. 11(a) shows the β phase precipitation and growth at triple junctions of α grain boundaries. Fig. 11(b) shows a heterogeneous GND distribution in which GNDs accumulate or are accommodated at grain boundaries. In particular, GNDs are observed to accumulate at the α/β boundary. As mentioned above, the GBS mechanism according to the Gifkins core–mantle model is dominant for an α/β Ti−6Al−4V alloy. In this case, the characteristics of the GND distribution in Fig. 11(b) indeed reveal that GBS occurs according to the Gifkins core–mantle model in the UFG Ti−6242S alloy. Thus, we found that the β phase effectively acted as an accommodation mechanism and contributed to enhanced GBS.

4.3. Load relaxation behavior and quantitative analysis of GBS

To analyze the relative contributions of grain matrix deformation (GMD) and GBS quantitatively, we evaluate the stress response as a function of strain rate assuming the GMD, GBS, and GMD + GBS curves according to the internal-variable theory of inelastic deformation [10,12,21–24]. Here, GMD is associated with deformation by dislocation glide, and GBS is accommodated mainly by a dislocation glide process. The constitutive equations for GMD and GBS are given by

$$\left(\frac{\sigma^*}{\sigma^I}\right) = \exp\left(\frac{\dot{\alpha}^*}{\dot{\alpha}}\right)^p \tag{4-2}$$

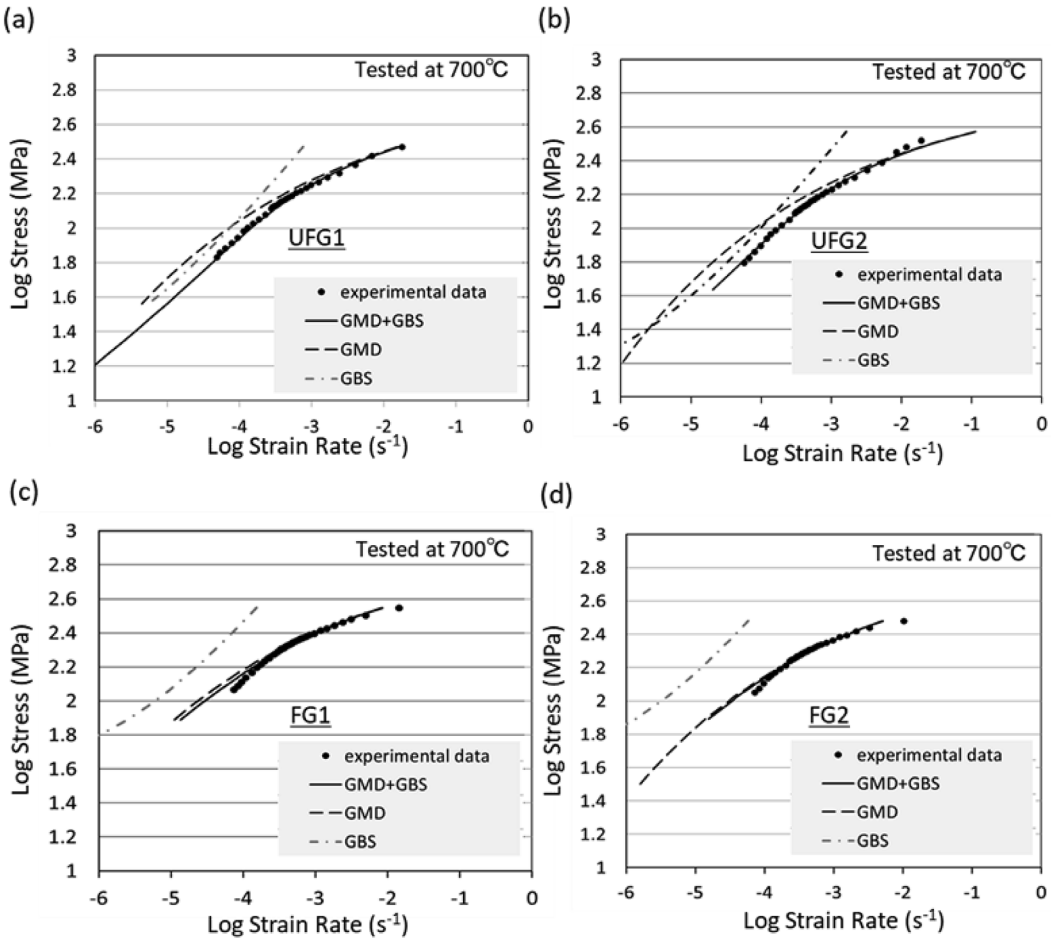

Fig. 12. Relationship between stress and strain rate in log–log scale at 700 °C according to Ref. [20] obtained by stress relaxation test of (a) UFG1 specimen, (b) UFG2 specimen, (c) FG1 specimen, and (d) FG2 specimen.

$$\left(\frac{\dot{g}}{\dot{g}_0}\right) = \left(\frac{\sigma}{\Sigma_g - 1}\right)^{1/Mg} \tag{4-3}$$

respectively, Here, σ^* and $\dot{\alpha}^*$represent the strength parameter and its conjugate reference strain rate, respectively, for GMD. Further, Σ_g and $\dot{g}_0$ represent the friction stress and its conjugate reference strain rate, respectively, for GBS. The exponents p and M_g are the material parameters for GMD and GBS, respectively. The variable σ^I in Eq. (4-2)represents the internal stress due to a long-range interaction force among dislocations. The variables $\dot{\alpha}$ and $\dot{g}$ correspond to the plastic strain rates due to GMD and GBS, respectively. These variables are evaluated to analyze the relative contributions of GMD and GBS.

Fig. 12 shows the relationship between the stress and strain rate in log–log scale for experimental data obtained at 700 °C and estimated curves based on the internal-variable theory of GMD [Eq. (4-2)], GBS [Eq. (4-3)], and GMD + GBS [Eqs. (4-2) and (4-3)]. The constitutive parameters, which were determined by optimization using nonlinear regression analysis, are listed in Table 4. Here, p and M_g are set to 0.15 and 0.5, respectively, on the basis of Refs. [10,23]. The parameter M_g is useful for understanding the GBS behavior described as a Newtonian or non-Newtonian viscous flow characterized by a power index M_g of 1.0 or 0.5 [21]. For the UFG1 and UFG2 specimens, the experimental data are well fitted by the estimated GMD curve at higher strain rates (more than 10^{-3} s^{-1}), whereas the experimental data and GMD curve obviously diverge at lower strain rates (less than 10^{-3} s^{-1}). This result implies that GBS is more frequently activated at strain rates of less than 10^{-3} s^{-1}. On the other hand, for the FG1 and FG2 specimens, the experimental data are well fitted by the estimated GMD curve at all strain rates ($\geq 10^{-4}$ s^{-1}), indicating that the deformation mode is dominated by dislocation glide. Additionally, the combined (GMD + GBS) curves deviate slightly from the experimental data at strain rates below 10^{-4} s^{-1}. This result suggests that in this region, the Harper–Dorn creep mechanism associated with dislocation-climb-controlled creep is activated.

Table 4
Constitutive parameters of the internal-variable theory for UFG and FG specimens at 700 and 800 °C.

	700 °C				800 °C		
	UFG1	UFG2	FG1	FG2	UFG1	UFG2	FG1
log σ*	2.85	2.83	2.93	2.89	2.40	2.34	2.54
log α*	−2.20	−2.09	−2.41	−2.43	−1.68	−1.62	−1.71
log Σ_g	1.10	1.06	1.57	1.57	1.05	0.95	1.22
log g_0	−5.82	−5.79	−5.68	−5.94	−4.32	−4.37	−4.58
p	0.15						
M_g	0.5						

Table 4 also shows the parameters for testing at 800 °C. Among these parameters, Σ_g is an important one that expresses the friction stress for GBS. The Σ_g values at 700 °C and 800 °C are lower for the UFG specimens than for the FG specimens, indicating that indeed GBS can easily operates by decreasing grain size in the initial microstructure. Furthermore, the Σ_g value at 700 °C and 800 °C of the UFG2 specimen is slightly lower than that of the UFG1 specimen, revealing that GBS occurs more easily in the UFG2 specimen. As discussed below, this is attributable to the effect of the higher fraction of the α/β interface region

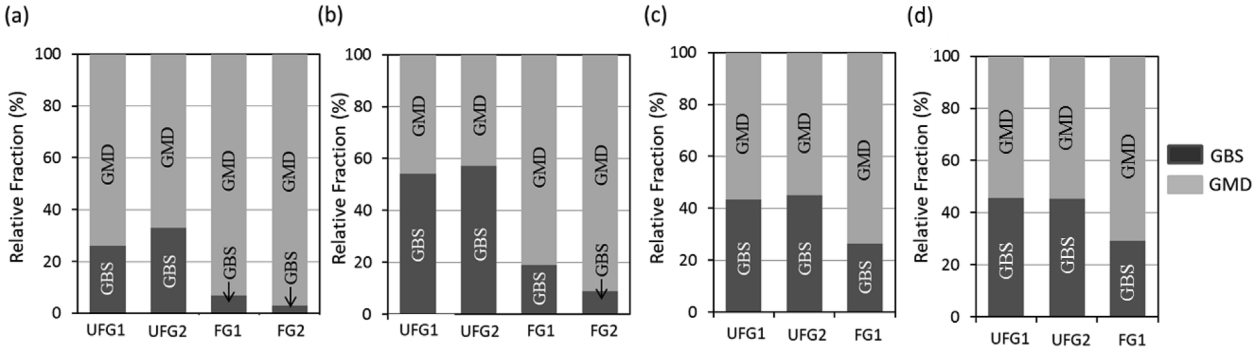

Fig. 13. Fraction of GMD and GBS relative to the overall deformation for the UFG1, UFG2, FG1, and FG2 specimens at (a), (b) 700 °C, and (c), (d) 800 °C and at strain rates of (a), (c) 10^{-3} s^{-1} and (b), (d) 10^{-4} s^{-1}.

in the UFG2 specimen.

The fraction relative to the overall strain/strain rate for the active deformation modes of GMD and GBS can be analyzed according to Fig. 12 and Table 4, as shown in Fig. 13. The UFG specimens exhibit a higher fraction of GBS at 700 °C than the FG specimens for strain rates of 10^{-3} and 10^{-4} s^{-1}. This result indicates that formation of UFG microstructure indeed contributes to the enhancement of GBS, resulting in higher tensile ductility. A previous report [10] revealed that the fraction of GBS in Ti−6242S alloy with a fine grain size of 2.2 μm was approximately 30% at 650 °C and 10^{-4} s^{-1} and approximately 40% at 750 °C and 10^{-4} s^{-1}. In comparison, the UFG specimens exhibit a higher fraction (more than 50%) for GBS activity at 700 °C and 10^{-4} s^{-1}, as shown in Fig. 13(b).

Specifically, the UFG2 specimen clearly shows slightly more GBS than the UFG1 specimen at 700 °C [Fig. 13(a) and (b)]. Additionally, the UFG1 and UFG2 specimens have almost the same fraction of GBS at 800 °C, as shown in Fig. 13(c) and (d). As mentioned above, in the UFG2 specimen, the amount of β precipitates exceeds the fraction at equilibrium, whereas the opposite is true for the UFG1 specimen. Considering the easier GBS at the α/β boundary [12,13], the above results indicate that GBS is more easily activated in the UFG2 specimen, especially at 700 °C. In contrast, we can judge that the α/β boundary has little effect at 800 °C.

To summarize, superplasticity appears at lower temperatures in the UFG Ti−6242S alloy. Specifically, at 700 °C, the UFG2 specimen shows more GBS than the UFG1 specimen owing to the effect of excess β precipitates in the initial microstructure of the UFG2 specimen. Furthermore, as mentioned above, dissociation of the β phase under deformation also contributes to the enhanced superplasticity. Thus, the obtained result suggests the possibility of further enhancement of superplasticity of Ti alloys via microstructural control not only by formation of UFG microstructure but also by excess β precipitation in the metastable initial microstructure by an optimized thermomechanical process and static heat treatment.

5. Conclusions

This work examined the effects of grain size, β fraction, and morphology on the deformation mode of Ti−6242S alloys. Five materials were prepared: the UFG1 specimen (having an equiaxed morphology with $d_\alpha = 0.78$ μm and $V_\beta = 2.8\%$), the UFG2 specimen (having an equiaxed morphology with $d_\alpha = 0.99$ μm and $V_\beta = 24.2\%$), the FG1 specimen (having an equiaxed morphology with $d_\alpha = 2.65$ μm and $V_\beta = 11.2\%$), the FG2 specimen (having an equiaxed morphology with $d_\alpha = 4.12$ μm and $V_\beta = 11.0\%$), and the STQ specimen (having acicular α′ martensite morphology). The UFG1 specimen was produced by hot-rolling of the STQ specimen with an acicular α′ martensite microstructure at 750 °C to approximately 1.3 mm. And the UFG2 specimen was produced by heat treatment of the UFG1 specimen at 400 °C. The FG1 specimen was as-received Ti−6242S alloy plate and the FG2 specimen was prepared by heat treatment of the FG1 specimen at 900 °C.

The obtained results are summarized as follows.

(1) The UFG specimens deformed in this work show lower flow stress and much higher elongation than the FG and STQ specimens. The strain rate sensitivity m reveals that the UFG specimens indeed exhibit superplasticity at lower temperatures. In the UFG specimens tested at 700 and 800 °C, the UFG2 specimen exhibits higher elongation at a higher strain rate (10^{-2} s^{-1}), whereas the UFG1 specimen exhibits higher elongation at a lower strain rate (10^{-4} s^{-1}). This behavior is attributable to the difference in the β fraction and the different accommodation mode activated under deformation, which is associated with decomposition of β from the initial metastable microstructure.

(2) With increasing strain under tensile deformation of the UFG specimens, the microstructure evolves into randomly oriented grains, accompanied by dynamic grain growth. In contrast, frequent activation of CDRX followed by GBS is observed in deformation of the FG specimens. These results indicate that GBS is the dominant deformation mode throughout deformation of the UFG specimens, whereas CDRX occurs once in the FG specimen in the initial and intermediate stages of deformation. During deformation of the UFG specimens, dynamic β precipitation occurs for the UFG1 specimen, and a decomposition process in which supersaturated β precipitates dissolve into the α phase occurs for the UFG2 specimen. This transformation behavior during deformation contributes to an additional accommodation mechanism for superplastic deformation. Analysis of the deformation mode according to the internal-variable theory reveals that more GBS occurs in the UFG2 specimen than in the UFG1 specimen, which is attributable to the effect of excess β precipitates in the initial microstructure of the UFG2 specimen. Thus, we found that enhanced superplasticity in the Ti−6242S alloy was achieved not only by forming UFG microstructure to enhance GBS but also by controlling the metastability of the initial microstructure to activate the accommodation mechanism frequently.

Acknowledgment

This research was partially supported by a Grant-in-Aid from the Japan Society for the Promotion of Science (JSPS, number 16H04537).

References

[1] G. Luetjering, J. Albrecht, A. Gysler, F.H. Froes, I. Caplan (Eds.), Titanium '92 Science and Technology, TMS, Warrendale, 1993, pp. 1635–1646.
[2] C. Andres, A. Gysler, G. Luetjering, F.H. Froes, I. Caplan (Eds.), Titanium '92 Science and Technology, TMS, Warrendale, 1993, pp. 311–318.
[3] G.B. Viswanathan, S. Karthikeyan, R.W. Hayes, M.J. Mills, "Creep behavior of Ti-6Al-2Sn-4Zr-2Mo: II. Mechanisms of deformation, Acta Mater. 50 (2002) 4965–4980.

[4] R.S. Mishra, V.V. Stolyarov, C. Echer, R.Z. Valiev, A.K. Mukherjee, Mechanical behavior and superplasticity of a severe plastic deformation processed nanocrystalline Ti–6Al–4V alloy, Mater. Sci. Eng., A 298 (2001) 44–50.
[5] Y.G. Ko, W.G. Kim, C.S. Lee, D.H. Shin, Microstructural influence on low-temperature superplasticity of ultrafine-grained Ti–6Al–4V alloy, Mater. Sci. Eng., A 410–411 (2005) 156–159.
[6] A.V. Sergueeva, V.V. Stolyarov, R.Z. Valiev, A.K. Mukherjee, Enhanced superplasticity in a Ti-6Al-4V alloy processed by severe plastic deformation, Scripta Mater. 43 (2000) 819–824.
[7] H. Matsumoto, K. Yoshida, S.H. Lee, Y. Ono, A. Chiba, Ti–6Al–4V alloy with an ultrafine-grained microstructure exhibiting low-temperature–high-strain-rate superplasticity, Mater. Lett. 98 (2013) 209–212.
[8] H. Matsumoto, T. Nishihara, V. Velay, V. Vidal, Superplastic property of the Ti–6Al4V alloy with ultrafine-grained heterogeneous microstructure, Adv. Eng. Mater. 20 (2018) 1700317, https://doi.org/10.1002/adem.201700317.
[9] M.T. Cope, D.R. Evetts, N. Ridley, Superplastic deformation characteristics of two microduplex titanium alloys, J. Mater. Sci. 21 (1986) 4003–4008.
[10] C.H. Park, B. Lee, S.L. Semiatin, C.S. Lee, Low-temperature superplasticity and coarsening behavior of Ti–6Al–2Sn–4Zr–2Mo–0.1Si, Mater. Sci. Eng., A 527 (2010) 5203–5211.
[11] T. Seshacharyulu, S.C. Medeiros, W.G. Frazier, Y.V.R.K. Prasad, Hot working of commercial Ti–6Al–4V with an equiaxed α–β microstructure: materials modeling considerations, Mater. Sci. Eng., A 284 (2000) 184–194.
[12] J.S. Kim, Y.W. Chang, C.S. Lee, Quantitative analysis on boundary sliding and its accommodation mode during superplastic deformation of two-phase Ti6Al4V alloy, Metall. Mater. Trans. 29 (1998) 217–226.
[13] S.M.L. Sastry, P.S. Pao, K.K. Sankaran, H. Kimura, O. Izumi (Eds.), Titanium '80, Science Technology, High Temperature Deformation of Ti-6Al-4V, vol. 2, AIME, New York, 1980, pp. 873–886.
[14] R.D. Doherty, D.A. Hughes, F.J. Humphreys, J.J. Jonas, D. Juul Jensen, M.E. Kassner, W.E. King, T.R. McNelley, H.J. McQueen, A.D. Rollett, Current issues in recrystallization: a review, Mater. Sci. Eng., A 238 (1997) 219–274.
[15] T. Furuhara, B. Poorganji, H. Abe, T. Maki, Dynamic recovery and recrystallization in titanium alloys by hot deformation, J. Occup. Med. 59 (2007) 64–67.
[16] S. Zherebtsov, M. Murzinova, G. Salishchev, S.L. Semiatin, Spheroidization of the lamellar microstructure in Ti–6Al–4V alloy during warm deformation and annealing, Acta Mater. 59 (2011) 4138–4150.
[17] F. Humphreys, M. Hatherly, Recrystallization and Related Annealing Phenomena, Elsevier, Oxford, 1995.
[18] J. Koike, Y. Shimoyama, I. Ohnuma, R. Kainuma, K. Ishida, K. Maruyama, Stress-induced phase transformation during superplastic deformation in two-phase Ti–Al–Fe alloy, Acta Mater. 48 (2000) 2059–2069.
[19] G. Yamane, V. Velay, V. Vidal, H. Matsumoto, Mechanical behavior of Ti-6Al-2Sn-4Zr-2Mo titanium alloy under hot and superplastic forming conditions: experiment and modeling, Defect Diffusion Forum 385 (2018) 413–418.
[20] D. Lee, E.W. Hart, Stress relaxation and mechanical behavior of metals, Metall. Trans. 2 (1971) 1245–1248.
[21] T.K. Ha, Y.W. Chang, Internal variable theory of structural superplasticity, Acta Metall. Mater. 46 (1998) 2741–2749.
[22] Y.N. Kwon, Y.W. Chang, The effect of grain size and temperature on the superplastic deformation behavior of a 7075 alloy, Metall. Mater. Trans. 30 (1999) 2037–2047.
[23] J.H. Kim, S.L. Semiatin, C.S. Lee, Constitutive analysis of the high-temperature deformation mechanisms of Ti–6Al–4V and Ti–6.85Al–1.6V alloys, Mater. Sci. Eng., A 394 (2005) 366–375.
[24] Y.G. Ko, C.S. Lee, D.H. Shin, S.L. Semiatin, Low-temperature superplasticity of ultrafine-grained Ti-6Al-4V processed by equal-channel angular pressing, Metall. Mater. Trans. 37 (2006) 381–391.
[25] H. Matsumoto, T. Nishihara, Y. Iwagaki, T. Shiraishi, Y. Ono, A. Chiba, Microstructural evolution and deformation mode under high-temperature-tensile-deformation of the Ti-6Al-4V alloy with the metastable α′ martensite starting microstructure, Mater. Sci. Eng., A 661 (2016) 68–78.
[26] H. Matsumoto, V. Velay, Mesoscale modeling of dynamic recrystallization, processing map characteristic, and room temperature strength of Ti-6Al-4V alloy forged in the (α + β) region, J. Alloy. Comp. 708 (2017) 404–413.
[27] R.W. Hayes, G.B. Viswanathan, M.J. Mills, Creep behavior of Ti–6Al–2Sn–4Zr–2Mo: I. The effect of nickel on creep deformation and microstructure, Acta Mater. 50 (2002) 4953–4963.
[28] S.L. Semiatin, G.A. Sargent, Constitutive modeling of low-temperature superplastic flow of ultrafine Ti-6Al-4V sheet material, Key Eng. Mater. 433 (2010) 235–240.
[29] J.S. Kim, J.H. Kim, Y.T. Lee, C.G. Park, C.S. Lee, Microstructural analysis on boundary sliding and its accommodation mode during superplastic deformation of Ti–6Al–4V alloy, Mater. Sci. Eng., A 263 (1999) 272–280.
[30] R.C. Gifkins, N.E. Paton, C.H. Hamilton (Eds.), Superplastic Forming of Structural Alloys, TMS-AIME, Warrendale, 1982, pp. 3–26.
[31] M.F. Ashby, The deformation of plastically non-homogeneous materials, Philos. Mag. A 21 (1970) 399–424.
[32] M. Calcagnotto, D. Ponge, E. Demir, D. Raabe, Orientation gradients and geometrically necessary dislocations in ultrafine grained dual-phase steels studied by 2D and 3D EBSD, Mater. Sci. Eng., A 527 (2010) 2738–2746.